Electronic Supplementary Information for

Resolving Local Reaction Environment toward an Optimized CO_2-to-CO Conversion Performance

Ke Ye,[1] Guiru Zhang,[1] Xian-Yin Ma,[2] Chengwei Deng,[3] Xin Huang,[1] Chonghao Yuan, [1] Guang Meng,[1] Wen-Bin Cai,[2] Kun Jiang[1,4,*]

[1] School of Mechanical Engineering, Shanghai Jiao Tong University, Shanghai 200240, China.

[2] Shanghai Key Laboratory of Molecular Catalysis and Innovative Materials, Collaborative Innovation Center of Chemistry for Energy Materials, Department of Chemistry, Fudan University, Shanghai 200433, China.

[3] State Key Laboratory of Space Power Sources Technology, Shanghai Institute of Space Power Sources, Shanghai 200245, China.

[4] Key Laboratory for Power Machinery and Engineering, Ministry of Education, Shanghai Jiao Tong University, Shanghai 200240, China

[*] To whom correspondence should be addressed: K.J. (Email: kunjiang@sjtu.edu.cn)

Contents

Computational fluid dynamics simulation on the flow field

In comparison to the dropwise electrolyte flow within traditional dual thin layer flow cell configuration, we set the catholyte flow rates effects (ranging from 1 to 128 mL min^{-1}) on the CO_2 mass transport and depletion rate within our customized DEMS flow cell via a Multiphysics simulation. The Reynolds-number is determined as 53 for 1 mL min^{-1}, 525 for 10 mL min^{-1}, 2627 for 50 mL min^{-1} and 6728 for 128 mL min^{-1}, respectively. Therefore, a laminar flow model is used to trace the first 2 flow patterns and a turbulent flow is used in the latter 2 cases.

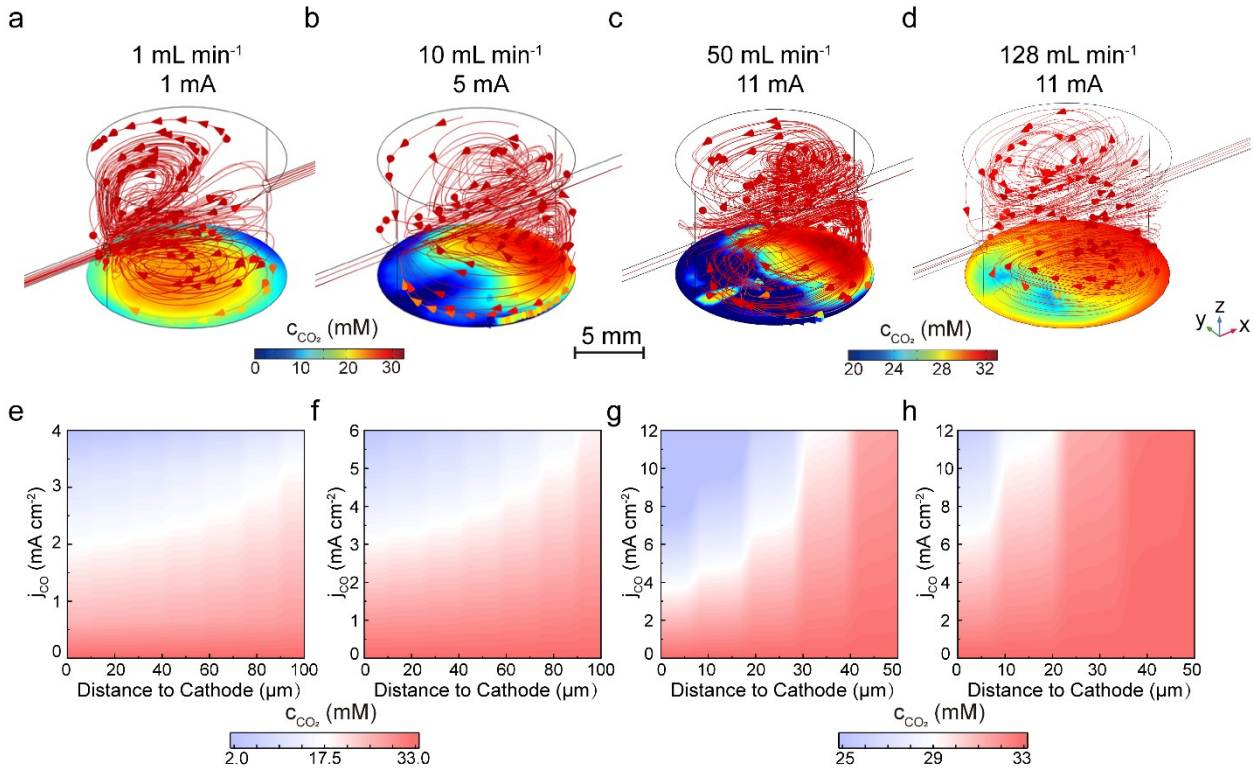

Fig. S1 Cathodic flow field simulation of customized DEMS cell at different flow rates and CO partial currents. (a-d) CO_2 flow streamline. (e-h) CO_2 distribution as the function of j_{CO} and distance to cathode. A facile CO_2 mass transport is visualized at relatively large catholyte flow rate, i.e., 50 to 128 mL min^{-1}, affordable to a large faradaic current and the relevant CO evolution reaction overriding the side reaction of H_2 evolution.

Residence time distribution (RTD) analysis in cathodic chamber

The residence time distribution of the catholyte was determined by a tracer method simulation in COMSOL Multiphysics v5.6 using two different boundary conditions. CO_2 is deployed as a tracer that diffuses at non-reaction condition, D_{CO2} is set as 1.91×10^{-9} $m^2 s^{-1}$.[1, 2]

Method 1: pulse input

The initial boundary condition of inlet concentration (c) and the flow rate (u) of tracer:

$$c_o = 33\ mM,\ u_0 = 4.3\ m\ s^{-1}\ (128\ mL\ min^{-1})$$

the bulk chamber and outflow of tracer:

$$c = 0, u = 0$$

the diffusion of tracer based on Fick's Law:

$$\frac{c_i}{t} + \nabla J_i + u \cdot \nabla c_i = 0$$

and

$$J_i = -D_i \nabla c_i$$

the outlet condition:

$$-nD_i \nabla c_i = 0$$

where ***n*** denotes the outward pointing normal of the boundary, other boundary conditions at the outer walls include no-slip and impermeable boundary. The residence time distribution function *E(t)* can be monitored at the outlet, and the integrated form as the cumulative distribution function *F(t)* (Figs. S2a-2c)

Method 2: step input

The initial boundary condition of inlet flux:

$$-nJ_i = 33(mM)$$

Other boundary conditions are the same as **Method 1** and the outlet tracer concentration is monitored as *F(t)*, together with the derivative *E(t)* as shown in Figs. S2d-2f.

The mathematical expectation, defined as the mean residence time (τ), is calculated as:

$$\tau = \int_0^\infty tE(t)dt$$

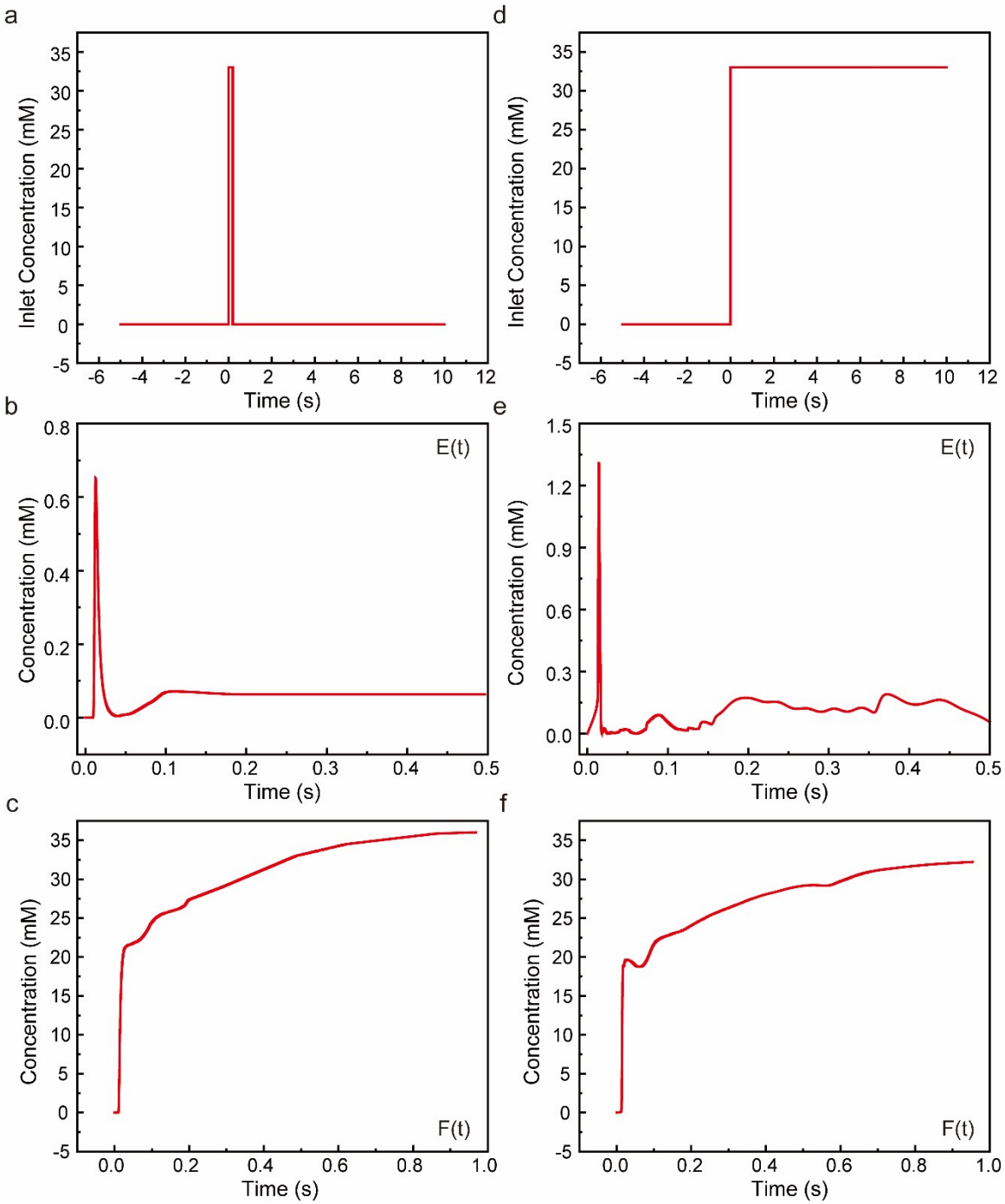

Fig. S2 Simulated residence time distribution in cathodic chamber using (a-c) pulse input method and (d-f) step input method.

DEMS signal responses during gas bubbling

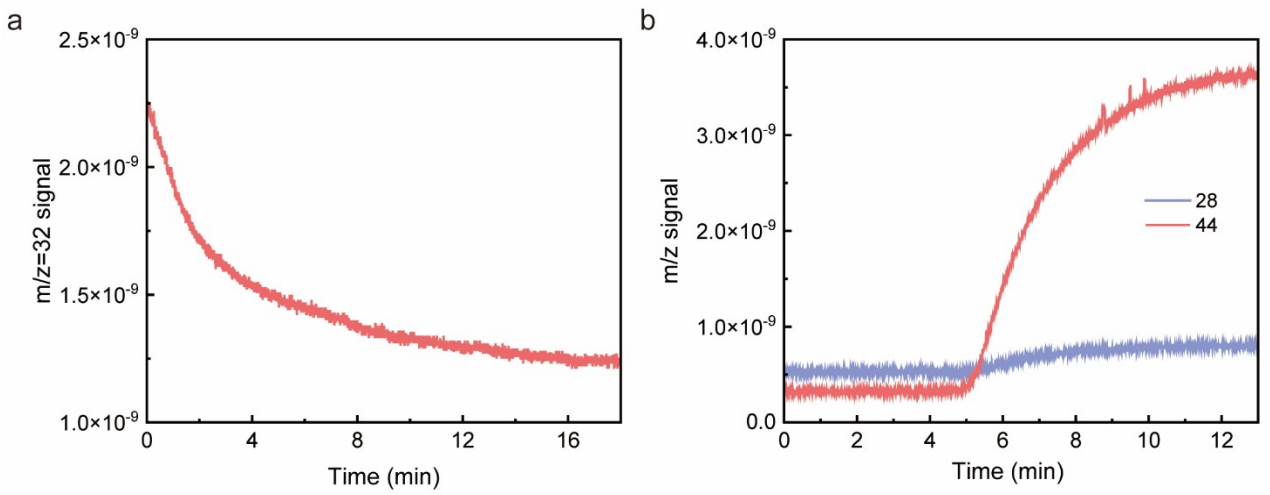

Fig. S3 DEMS signals recorded during (a) the deaeration by Ar purging and (b) CO_2 bubbling within 0.05 M K_2CO_3. O_2 signal of m/z=32 is monitored as the representative of deaeration process, while both signals of m/z=28 and 44 correspond to CO_2 species.

SEM images of Ag/CFP

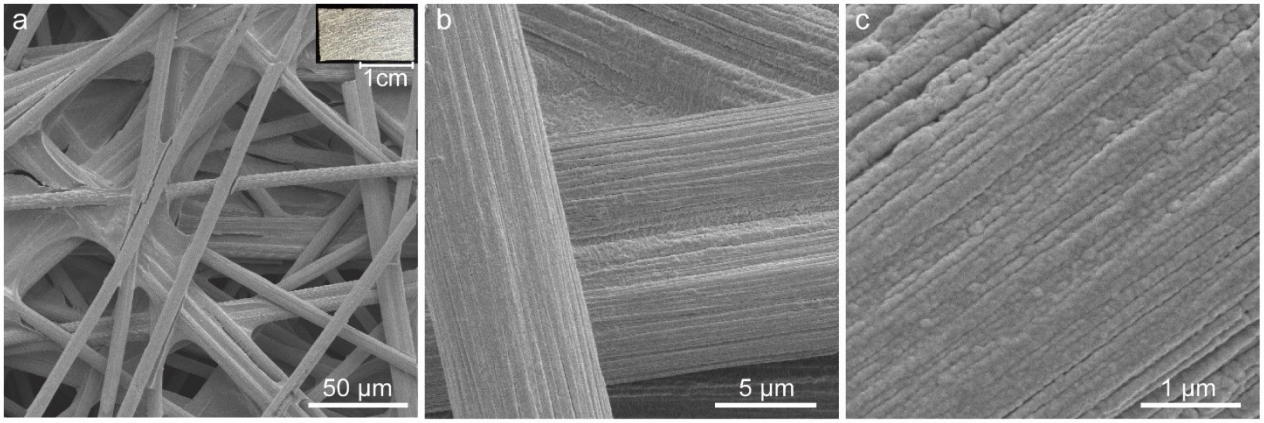

Fig. S4 Surface morphology characterization of sputtered Ag/CFP electrode by SEM at different magnification. Insert shows the photograph of 1×2-cm^2 Ag/CFP.

On-line gas chromatography calibration

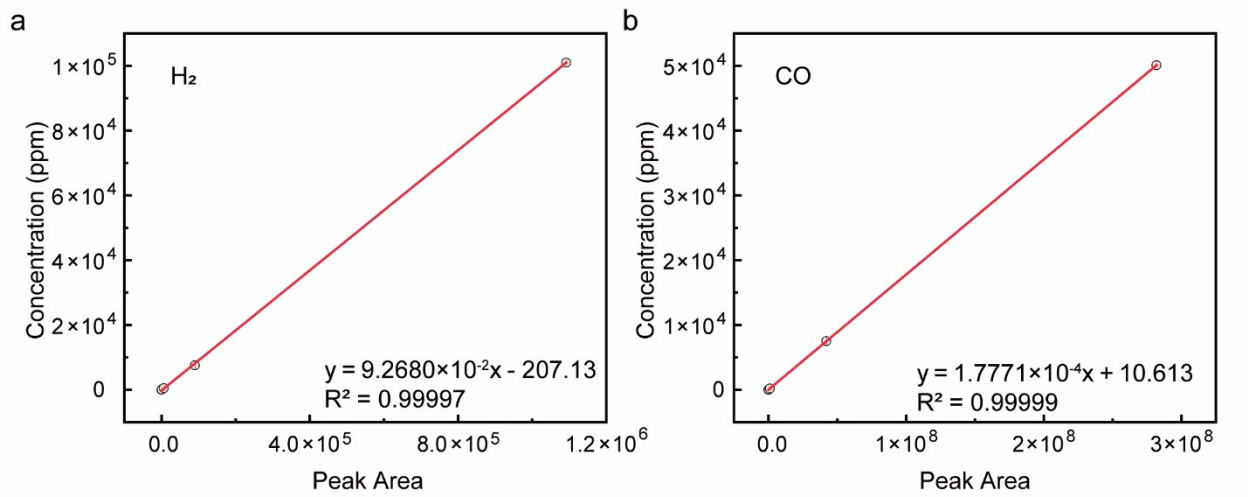

Fig. S5 GC calibration curves for (a) H_2 (concentrations ranging from 50.6 to 101000 ppm) and (b) CO (concentrations ranging from 20.3 to 50100 ppm). The error bars illustrate the standard deviation from at least three independent measurements.

Partial current densities as measured by on-line GC connected to H-cell electrolyzer

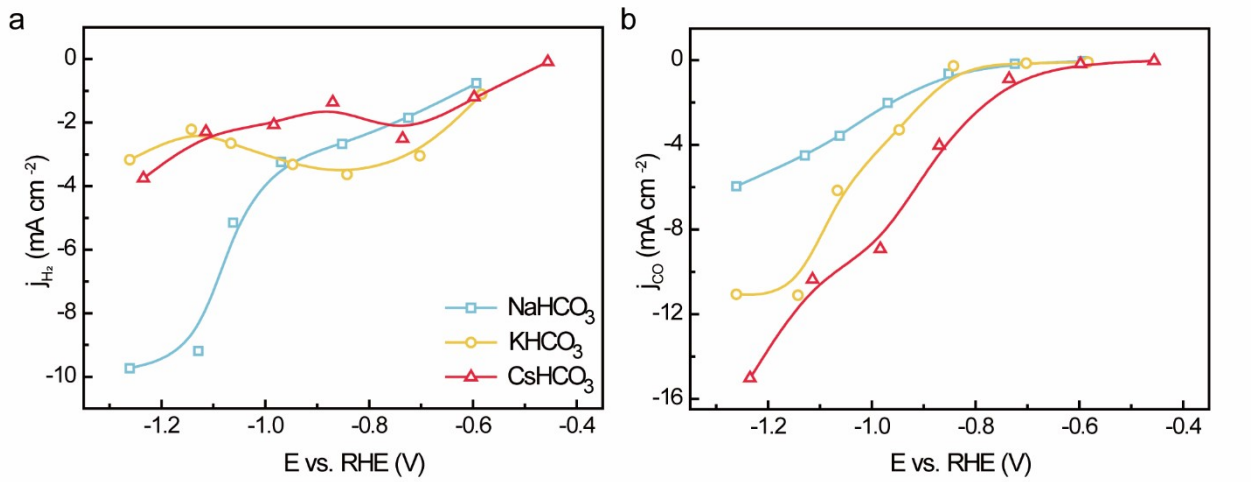

Fig. S6 Partial current density for (a) H_2 and (b) CO as derived from Ag/CFP catalyzed CO_2RR within H-cell electrolyzer containing 0.1 M CO_2-saturated $MHCO_3$.

DEMS raw data

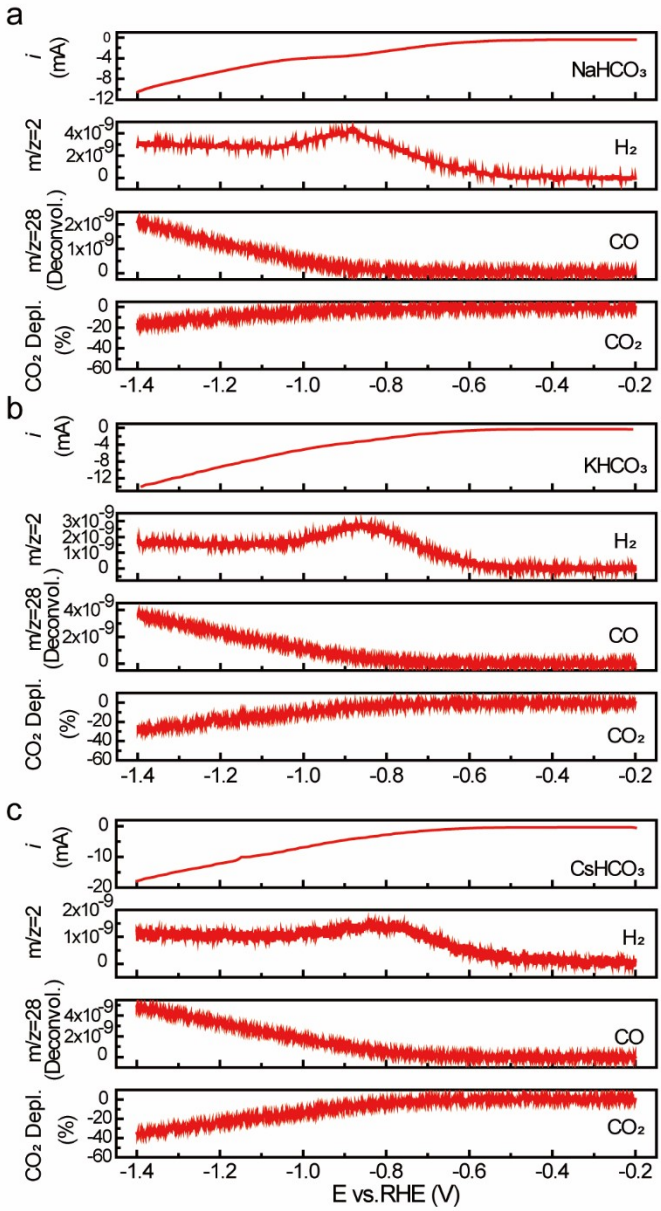

Fig. S7 DEMS raw data acquired simultaneously with LSV scan from -0.2 V to -1.4 V, the background baseline has been subtracted from DEMS signals toward the products quantification.

Standard mass spectra and signal deconvolution for CO_2 and CO.

Pure reactant of CO_2 and product of CO species were bubbled into 0.05 M Cs_2CO_3 electrolyte till saturation, their standard mass spectra were recorded during electrolyte circulation and in good agreement with NIST standards.[3, 4]

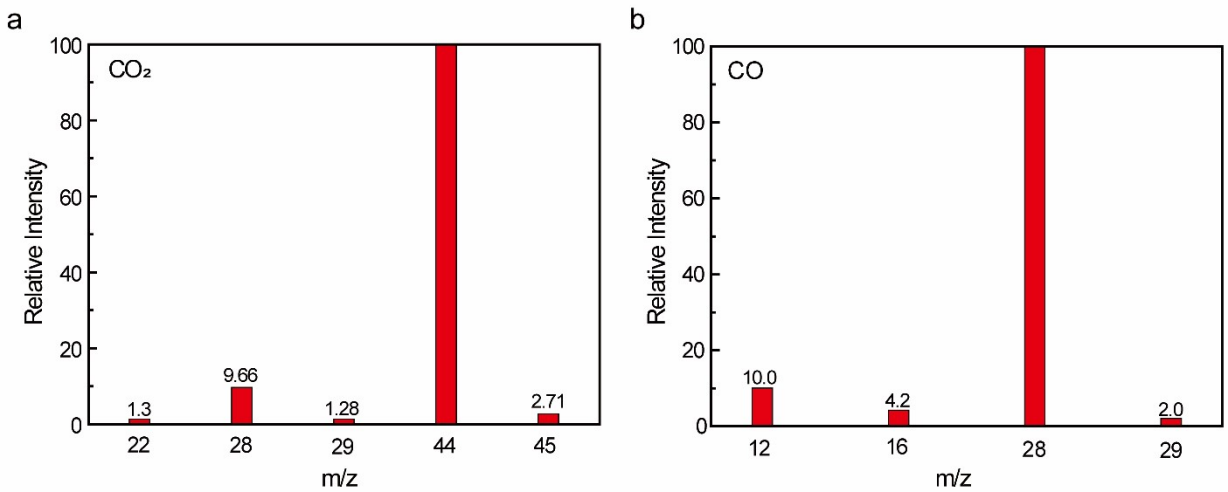

Fig. S8 Histogram of standard mass spectra for (a) CO_2 and (b) CO. For CO product quantification, ca. 9.66% signal of m/z=44 should be subtracted from CO_2 interference.

CO_2 consumption rate and ratio derived from GC and DEMS results

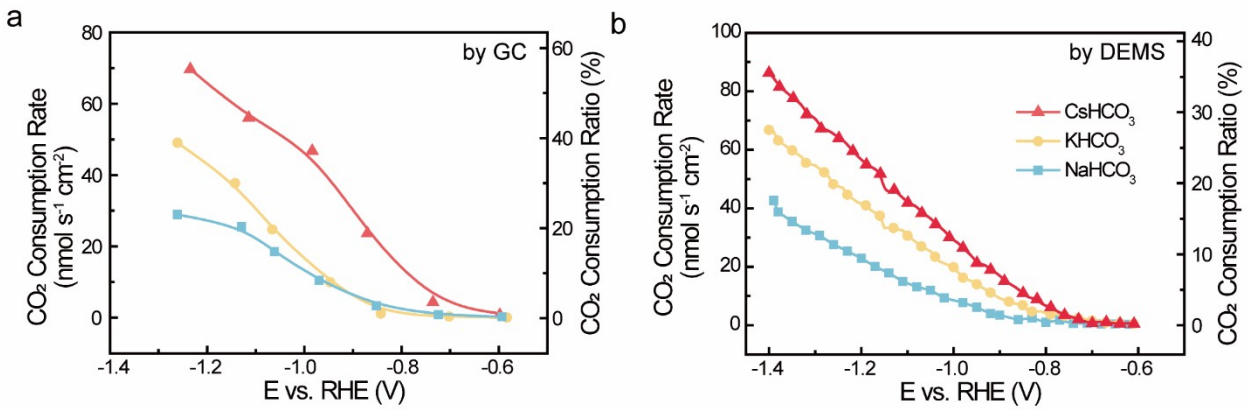

Fig. S9 CO_2 consumption rate and consumption ratio as a function of applied voltage in (a) gas-tight H-type cell deployed in online GC measurements and (b) flow cell electrolyzer deployed in DEMS measurements.

In a typical H-cell measurement, 50 sccm CO_2 was fed into the cathodic chamber under stirring, leading to a hydrodynamic boundary layer thicknesses of ~50 μm[5, 6] and a corresponding diffusion limited CO_2 flux of ~126 nmol s^{-1} cm^{-2} using Fick's Law[7]. While for DEMS measurements, the CO_2 consumption ratio can be directly visualized by tracking the mass-ion signal of 44.

Chronoamperometric DEMS results during different electrolyte switching.

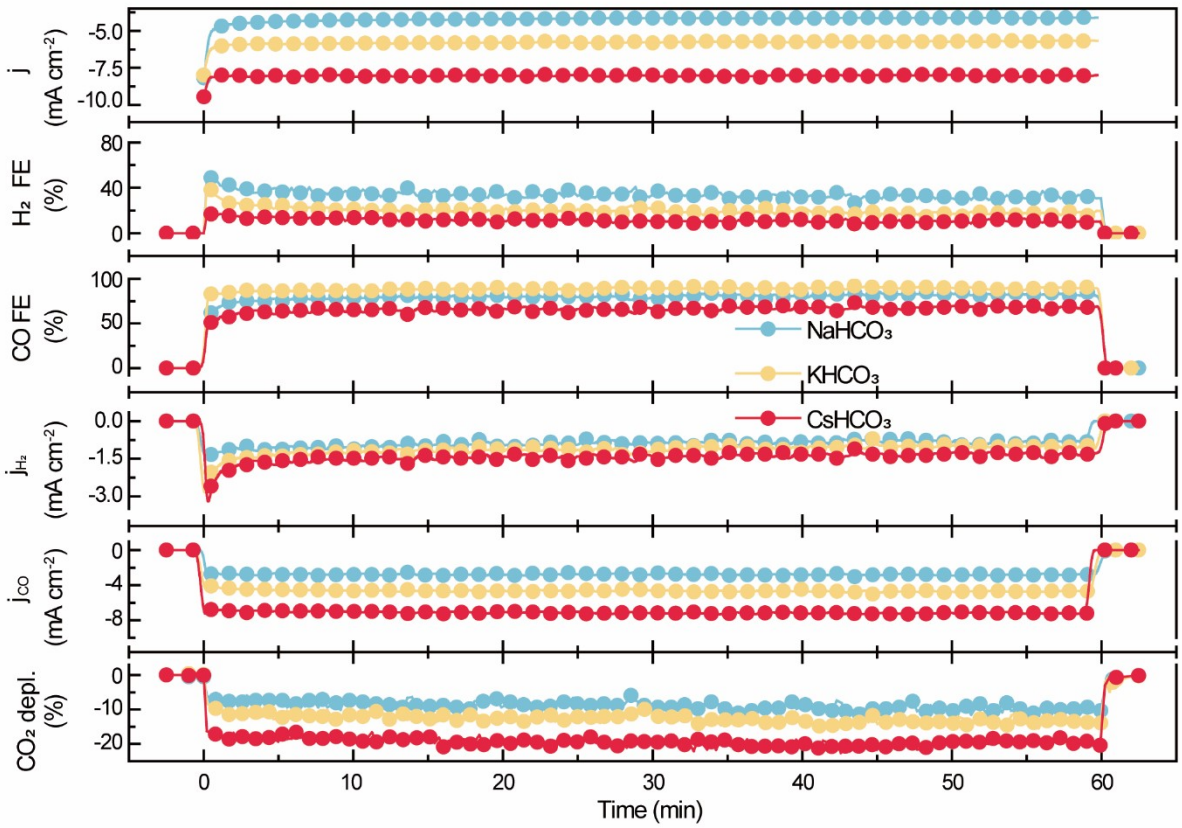

Fig. S10 Faradaic currents and relevant DEMS results as measured from 1-h chronoamperometric test within 0.1 M CO_2-saturated $MHCO_3$ electrolytes at -1.1 V.

Table S1. Calculated surface pH and recorded CO_2RR performance at given potentials.

E vs. RHE	Cation	*j* (mA cm^{-2})	Surface pH*	CO FE (%)	Depleted CO_2
-0.8 V	Na^+	-2.34	7.80	11.6	-1.9%
	K^+	-2.27	7.79	27.4	-3.7%
	Cs^+	-2.55	7.83	47.4	-4.3%

* The surface pH was estimated assuming a hydrodynamic boundary layer thickness of ~30 μm in DEMS flow cell and a bicarbonate concentration of 0.1 M.[1, 8]

Cation effect on the formation rates of H_2 and CO products.

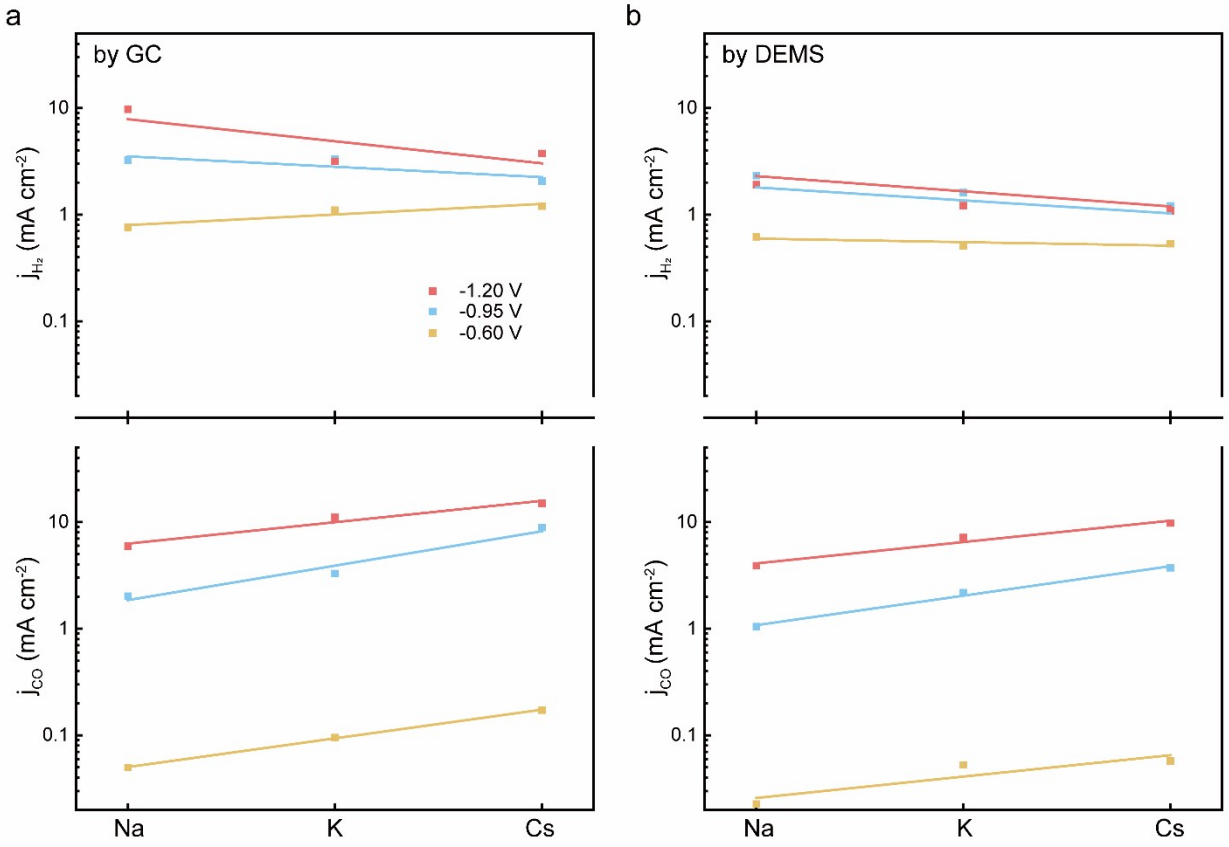

Fig. S11 Partial current densities for H_2 and CO products as a function of the electrolyte metal cation, the data are derived from (a) online GC and (b) DEMS measurements, respectively. Notably, the DEMS results are recorded on a same Ag/PTFE electrode upon different electrolyte switching, ensuring a more accurate comparison.

SEM images of O_2 plasma bombarded Ag/CFP.

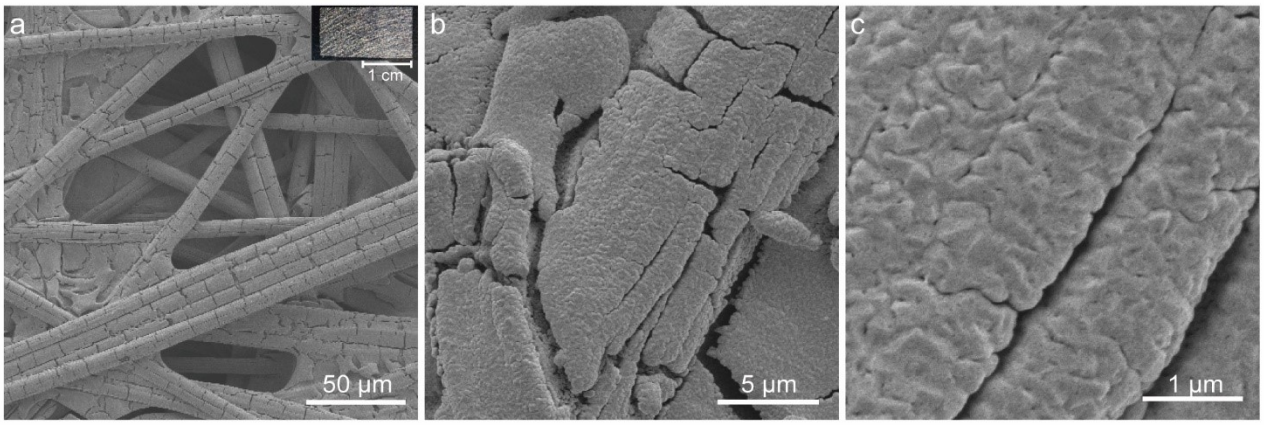

Fig. S12 Surface morphology characterization of O_2 plasma bombarded Ag/CFP electrode by SEM at different magnification. Insert shows the photograph of 1×2-cm^2 Ag/CFP after 150-s plasma treatment, for which the color changes from silvery (Fig. S4) to dark grey.

Surface roughness assessment by electrochemical double layer capacitance (EDLC) measurement.

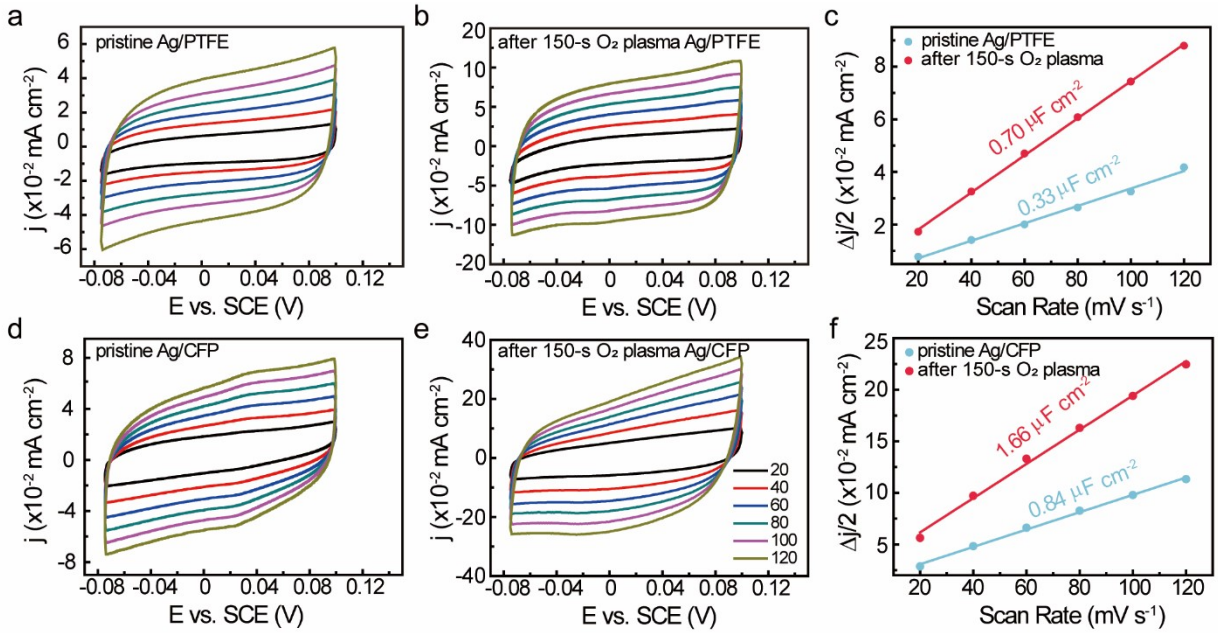

Fig. S13 Electrochemical double layer capacitance measurements and relevant surface roughness assessment for (a-c) Ag/PTFE and (d-f) Ag/CFP electrodes before and post 150-s O_2 plasma bombardment. Cyclic voltammetry was performed in the non-reaction potential window at a series of increasing scan rates from 20, 40, 60, 80, 100 to 120 mV s^{-1} to determine the EDLCs.

Surface components analysis by XPS.

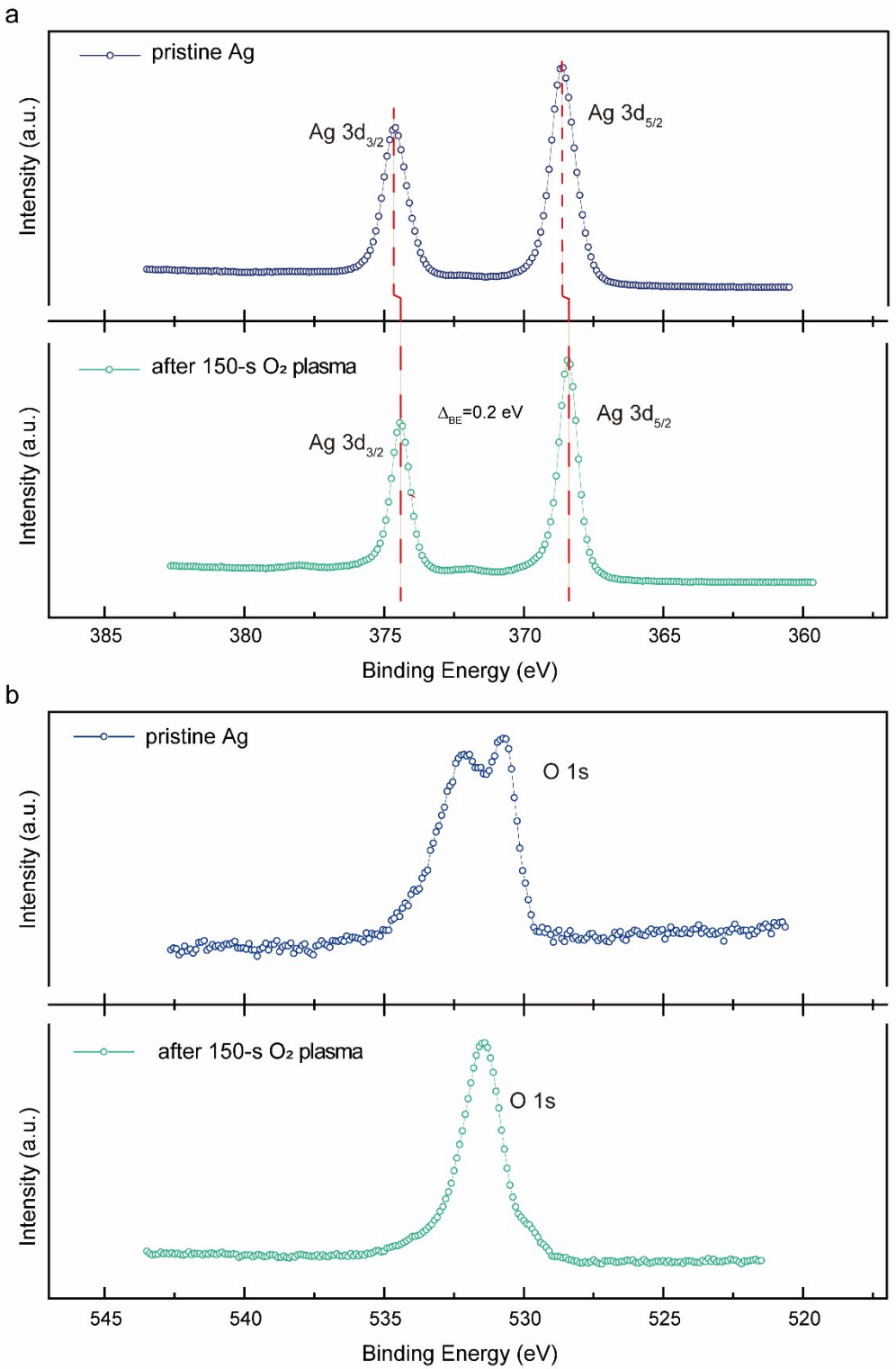

Fig. S14 Core-level XPS spectra on (a) Ag 3d region and (b) O 1s region for the pristine (blue line) and post O_2 plasma treated (green line) Ag/PTFE electrode.

Pre-reduction of O_2 plasma bombarded Ag/PTFE.

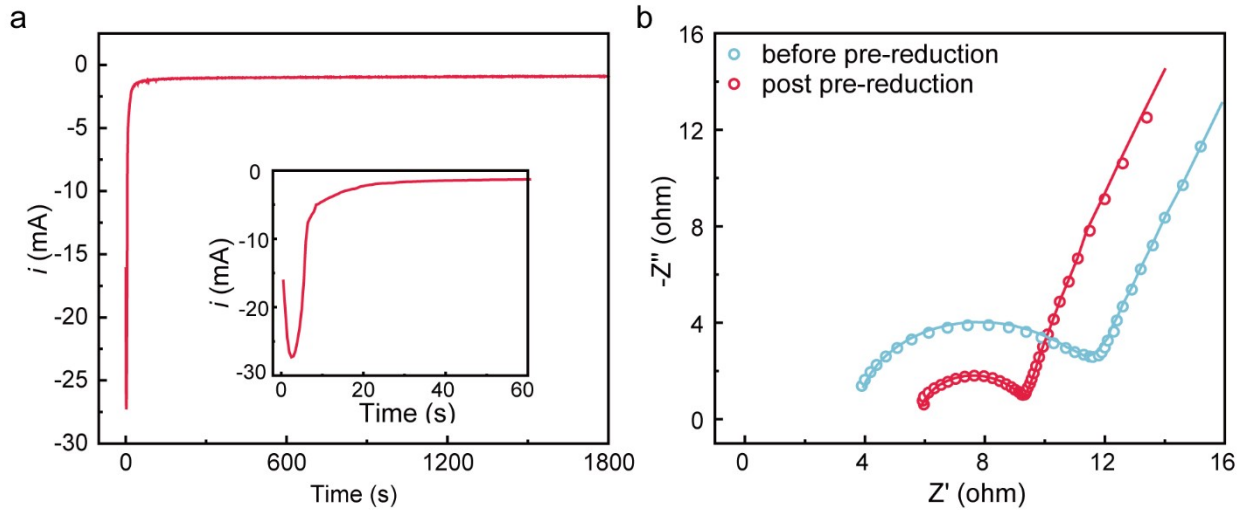

Fig. S15 Pre-reduction of Ag/PTFE electrode subject to 150-s O_2 plasma pre-treatment. (a) *i-t* curve recorded during the pre-reduction process at -0.54 V vs. RHE in 0.1 M CO_2-saturated $NaHCO_3$, (b) relevant Nyquist plots recorded at open circuit potentials with the frequency ranging from 0.1 Hz to 200 kHz.

The topology effect of plasma pretreated Ag as probed by DEMS.

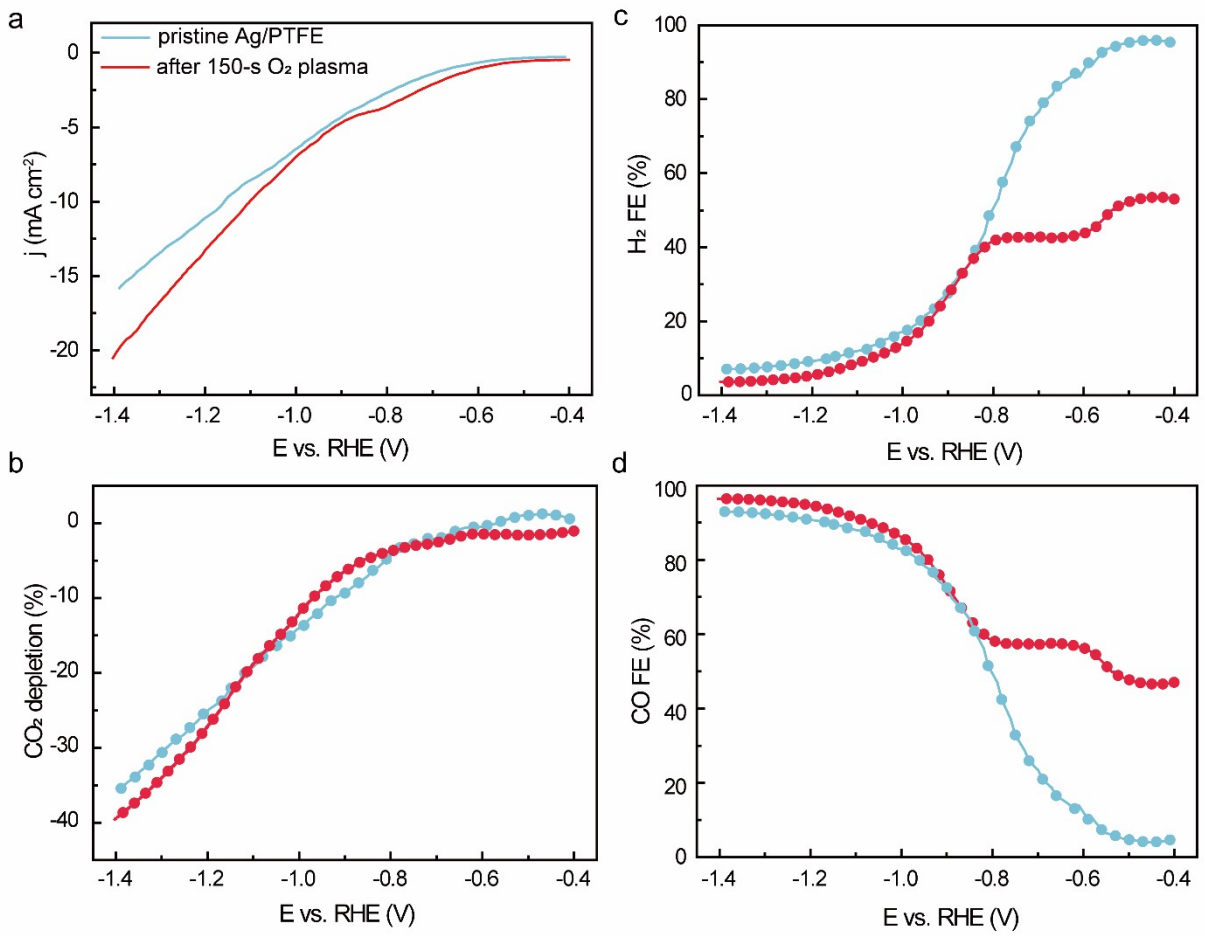

Fig. S16 Comparative DEMS results on electrochemical CO_2RR performance recorded over pristine Ag/PTFE and that after O_2 plasma treatment.

The topology effect of plasma pretreated Ag as probed by on-line GC.

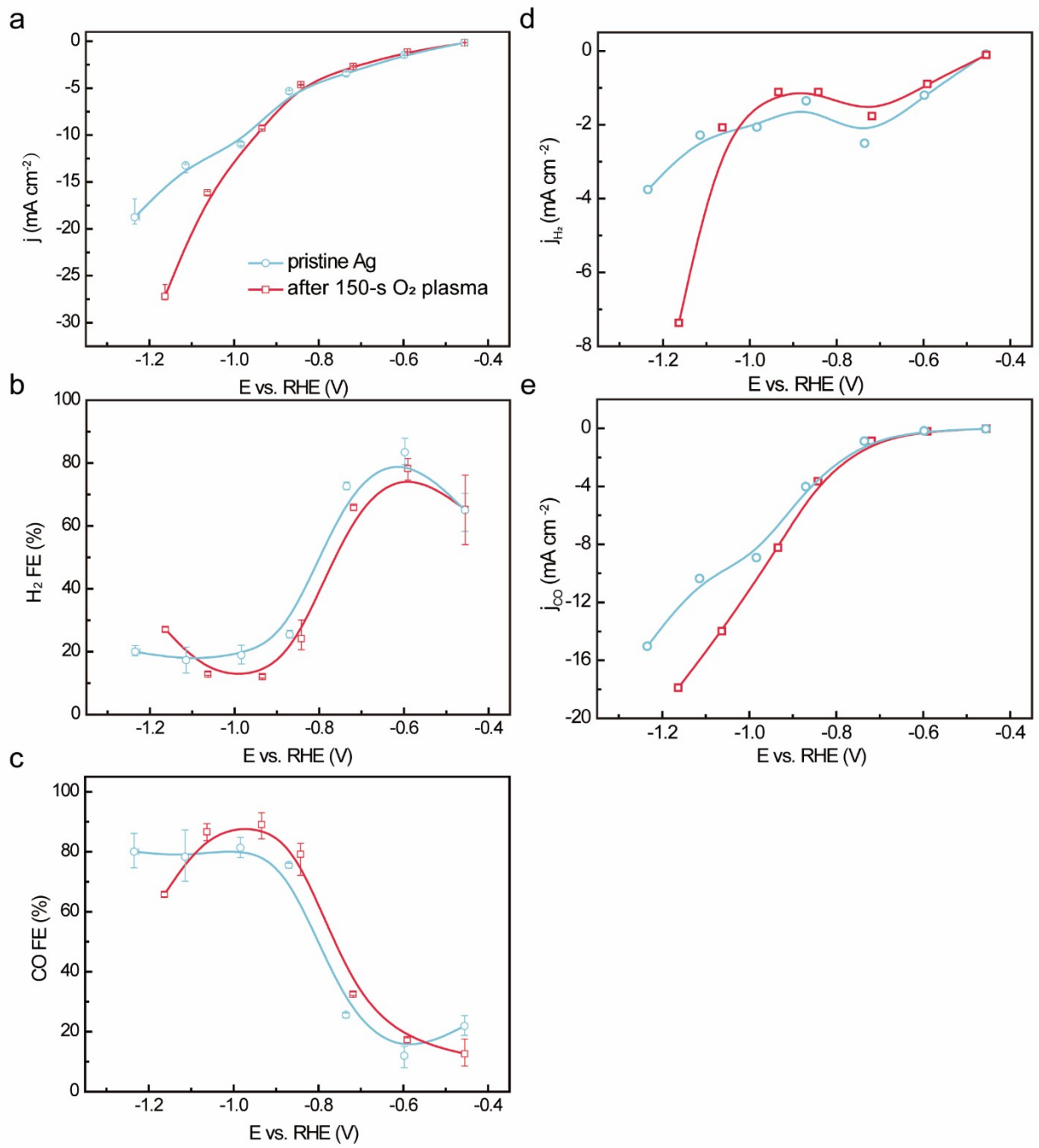

Fig. S17 Comparative on-line GC results on electrochemical CO_2RR performance recorded over pristine Ag/CFP and that post O_2 plasma treatment.

Tafel slope on Ag electrode before and after 150-s O_2 plasma pre-treatment.

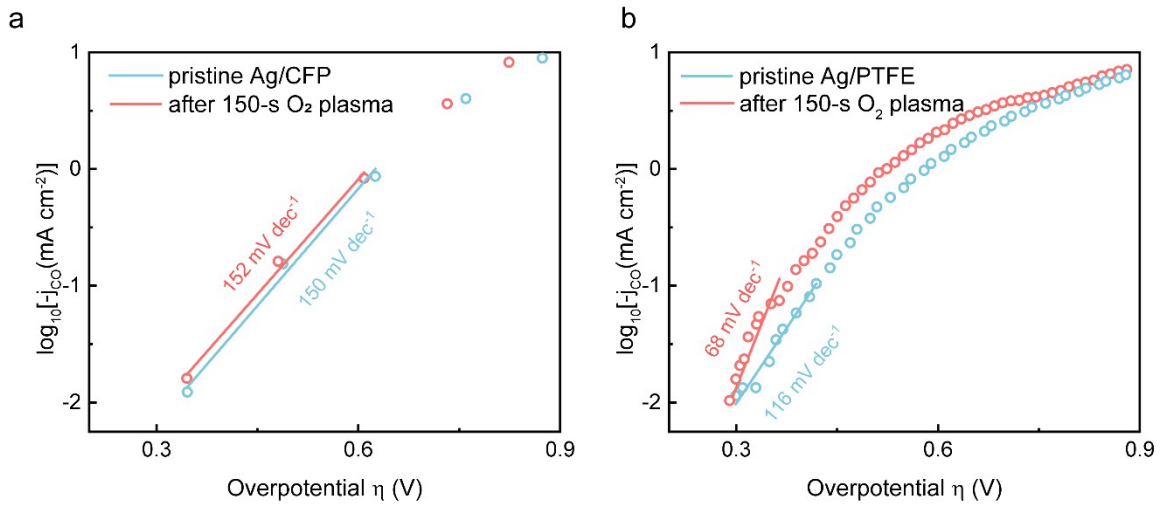

Fig. S18 Tafel plots for (a) Ag/CFP and (B) Ag/PTFE electrodes with or without 150-s O_2 plasma pre-treatment.

In a typical H-cell measurement with GC quantification, a similar Tafel slope of ~150 mV dec^{-1} between the two electrodes is observed, which is probably due to the large potential window from -0.42 to -0.72 V vs. RHE that beyond kinetic-controlled regime[9]. In contrast, a much denser data points with higher time resolution (or potential resolution) are recorded during DEMS measurement, which could ensure a more accurate evaluation on the reaction kinetics.

Schematic of the completed MEA electrolyzer system.

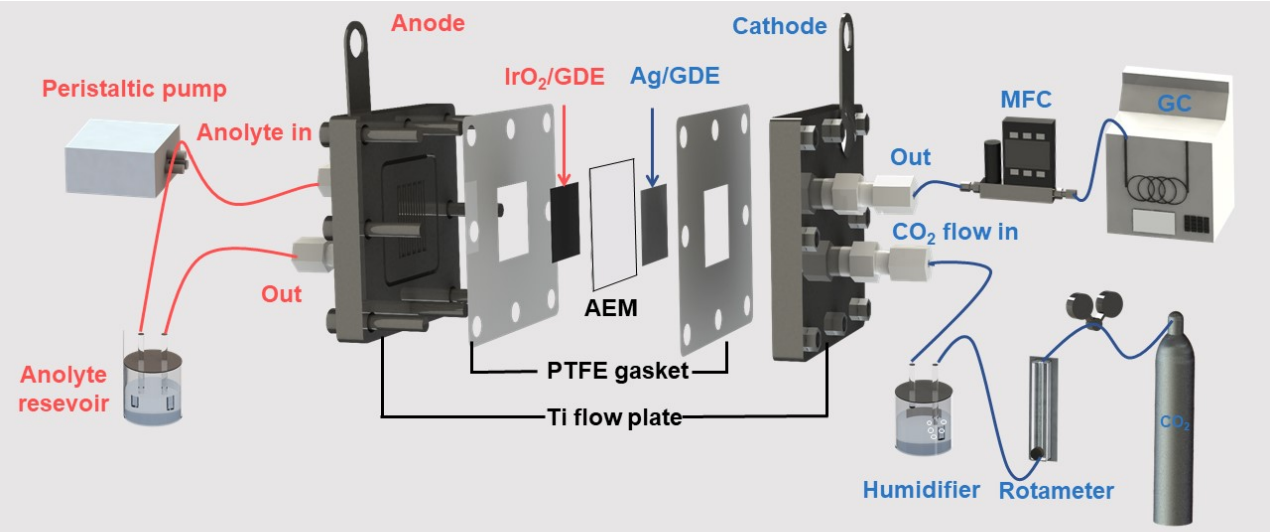

Fig. S19 Schematic of the completed MEA electrolyzer system, the details of MEA configuration are depicted in Fig. 5a and Methods section of main text. At anode side, the anolyte flow rate was set as 1.8 mL min^{-1} and controlled by a peristaltic pump, while only humidified CO_2 was fed to cathode side without catholyte circulation. To avoid the overestimation of Faradaic efficiency from CO_2 crossover and consumption, an upstream rotameter is used for roughly control the cathodic CO_2 flow rate and the effluent is delivered into the GC for quantitative analysis at a rate of 100 sccm as monitored by a Alicat mass flow controller. In a typical operation, the effluent pressure could be maintained below ~15.1 psi.

Table S2 Performance summary on CO_2-to-CO conversion in reported MEA electrolyzers.

Catalysts	Activity			Stability			References
	CO FE (%)	Voltage (V)	*j* (mA cm^{-2})	*j* (mA cm^{-2})	CO FE (%)	Operation Hours	
Ag	**92**	**3**	**150**	**500**	**> 80**	**100**	**This work**
	76	**4**	**867**				
Ag[10]	90	3.5	720	450	90%	200	*Nat. Energy* **6**, 439-448 (2021).
Ag-NP[11]	93.5	3.8	230	160	90%	18	*ACS Energy Lett.* **6**, 809-815 (2021).
	77.4	4.2	440				
e-Ag coral[12]	90	3.5	350	100	>70	30	*Nano Energy* **76** (2020).
Ag-NP[13]	80	2.7	200	-	-	-	*ACS Energy Lett.* **5**, 1612-1618 (2020).
Ag-NP[14]	85	3.4	740	500	80	100	*Energy Environ. Sci.* **13**, (2020).
Ag[15]	96.7	3	200	200	97	10	*J. CO_2 Util.* **31**, 244-250, (2019).
	90	3.2	420				
Ag[16]	98	3.3	200	-	-	-	*ACS Appl. Mater. Interfaces* **11**, 41281-41288, (2019).
Ag-NP[17]	95	3	300	200	65	8	*ACS Energy Lett.* **4**, 1770-1777, (2019).
Ag[18]	80	4.7	300	300	60%	1200	*Nat. Catal.* **1**, 32-39 (2018).
Ag[19]	98	3	200	200	98	4000	*J. Electrochem. Soc.***165**, (2018).
Ag[20]	98	3	150	50	95	4380	*Energy Technol.* **5**, 929-936, (2017).
Pd/C[21]	98	3.2	200	100	98	40	*Sci. China Chem.* **63**, 1711-1715, (2020).
Ni-NCB[22]	~100	2.7	130	100	~100	20	*Joule* **3**, 265-278, (2019).
Au[23]	90	3	500	100	95	100	*Energy Environ. Sci.***12**, 2455-2462, (2019).
CoPc[23]	90	2.8	200	-	-	-	
Ni–NG[24]	90	2.8	50	50	90	8	*Energy Environ. Sci.* **11**, 893-903, (2018).

Performance map on CO_2-to-CO conversion in reported MEA electrolyzers.

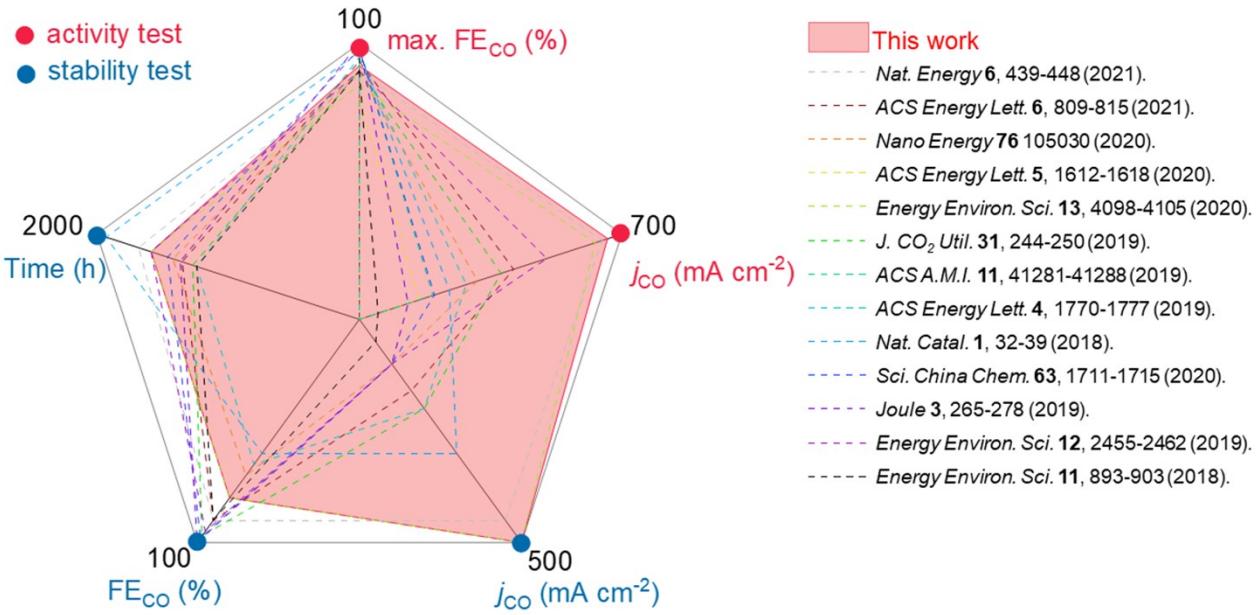

Fig. S20 Performance map of CO_2-to-CO conversion in reported MEA electrolyzers.

Anolyte effect on MEA electrolyzer performance

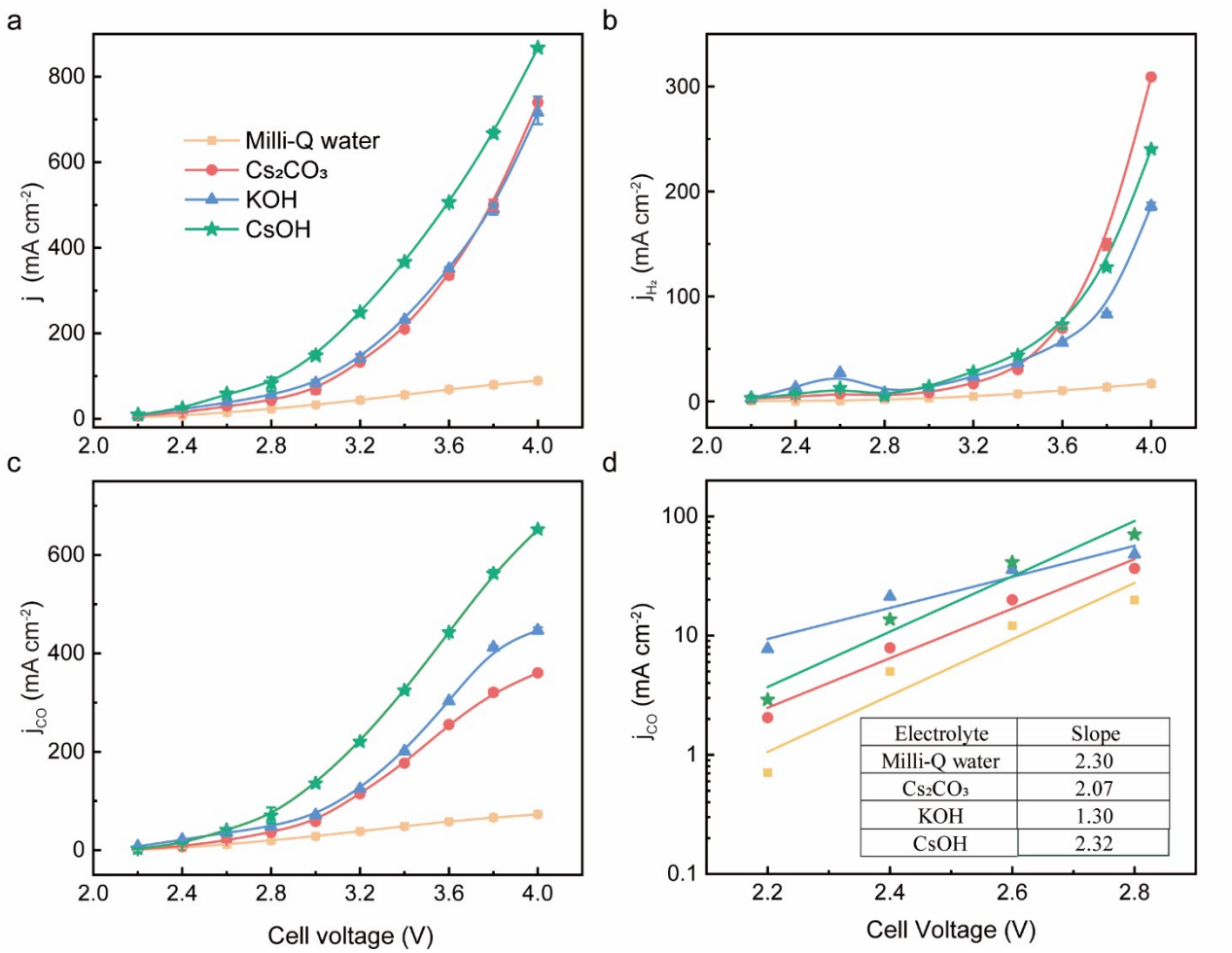

Fig. S21 Performance comparison by circulating different anolytes in the MEA electrolyzer. The molar concentration of Cs_2CO_3, KOH and CsOH are fixed at 0.01 M for comparison. Similar to those in DEMS flow cell and H-cell tests, a more facile CO evolution kinetics is observed with CsOH anolyte even in this anion exchange membrane reactor, which is probably due to the inevitable cation cross-over through the membrane.[10]

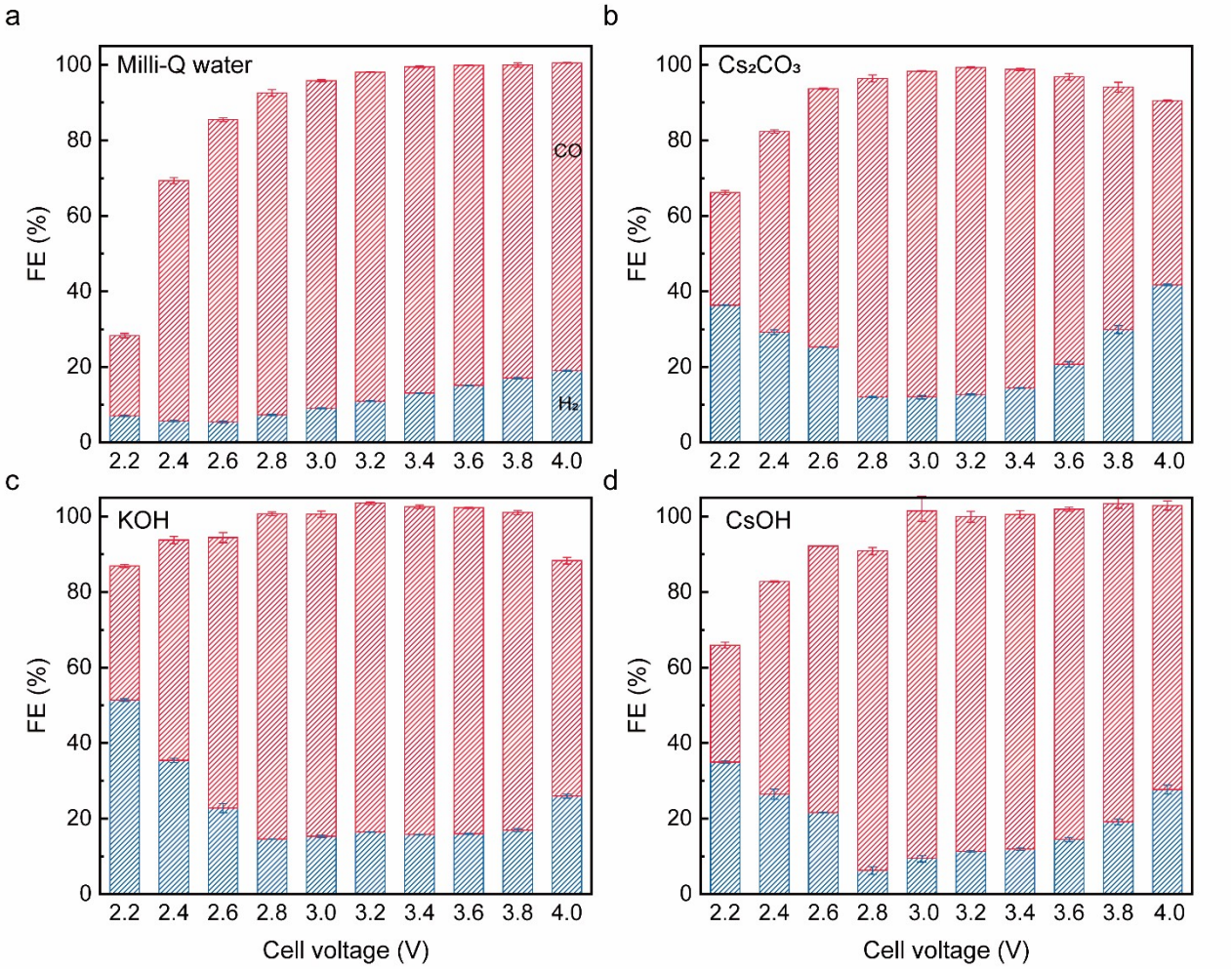

Fig. S22 Histogram of determined FEs for CO (red) and H_2 (blue) within different anolytes. (a) Milli-Q water, (b) 10 mM Cs_2CO_3, (c) 10 mM KOH and (d) 10 mM CsOH.

Characterizations on cathodic flow plate and Ag/GDE before and post 100-h electrolysis.

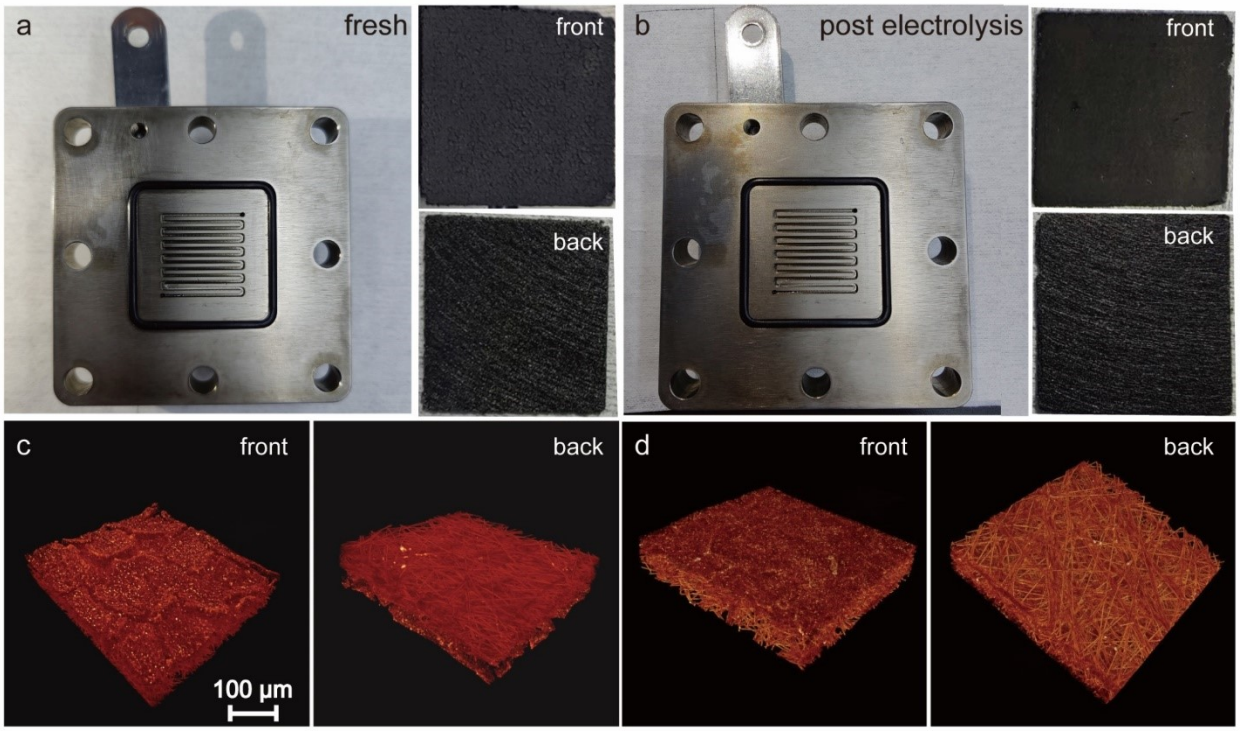

Fig. S23 Topology characterization of cathodic flow plate and Ag/GDE in MEA electrolyzer. Photos of flow panel and gas diffusion electrode taken (a) before electrolysis and (b) post 100-h continuous operation, relevant MicroCT topographic characterizations are shown in panel (c) and (d), respectively. No salt precipitation was observed neither within the flow panel nor within the gas diffusion electrode after the long-term operation.

References

1. L. C. Weng, A. T. Bell and A. Z. Weber, *Phys. Chem. Chem. Phys.*, 2018, **20**, 16973-16984.
2. E. L. Clark, M. R. Singh, Y. Kwon and A. T. Bell, *Anal. Chem.*, 2015, **87**, 8013-8020.
3. Standard mass spectra of CO_2 in NIST, https://webbook.nist.gov/cgi/cbook.cgi?ID=C124389&Units=SI&Mask=200.
4. Standard mass spectra of CO in NIST, https://webbook.nist.gov/cgi/cbook.cgi?ID=C630080&Units=SI&Mask=200#Mass-Spec.
5. E. L. Clark, J. Resasco, A. Landers, J. Lin, L.-T. Chung, A. Walton, C. Hahn, T. F. Jaramillo and A. T. Bell, *ACS Catal.*, 2018, **8**, 6560-6570.
6. A. S. Malkani, J. Li, J. Anibal, Q. Lu and B. Xu, *ACS Catal.*, 2019, **10**, 941-946.
7. D. Raciti, M. Mao and C. Wang, *Nanotechnology*, 2018, **29**.
8. J. E. Huang, F. Li, A. Ozden, A. S. Rasouli, F. P. G. de Arquer, S. Liu, S. Zhang, M. Luo, X. Wang and Y. Lum, *Science*, 2021, **372**, 1074-1078.
9. M. Dunwell, W. Luc, Y. Yan, F. Jiao and B. Xu, *ACS Catal.*, 2018, **8**, 8121-8129.
10. B. Endrodi, A. Samu, E. Kecsenovity, T. Halmagyi, D. Sebok and C. Janaky, *Nat. Energy*, 2021, **6**, 439-448.
11. Y. Xu, J. P. Edwards, S. Liu, R. K. Miao, J. E. Huang, C. M. Gabardo, C. P. O'Brien, J. Li, E. H. Sargent and D. Sinton, *ACS Energy Lett.*, 2021, **6**, 809-815.
12. W. H. Lee, Y.-J. Ko, Y. Choi, S. Y. Lee, C. H. Choi, Y. J. Hwang, B. K. Min, P. Strasser and H.-S. Oh, *Nano Energy*, 2020, **76**, 105030.
13. A. Reyes, R. P. Jansonius, B. A. W. Mowbray, Y. Cao, D. G. Wheeler, J. Chau, D. J. Dvorak and C. P. Berlinguette, *ACS Energy Lett.*, 2020, **5**, 1612-1618.
14. B. Endrődi, E. Kecsenovity, A. Samu, T. Halmágyi, S. Rojas-Carbonell, L. Wang, Y. Yan and C. Janáky, *Energy Environ. Sci.*, 2020, **13**, 4098-4105.
15. J. Lee, J. Lim, C.-W. Roh, H. S. Whang and H. Lee, *J. CO_2 Util.*, 2019, **31**, 244-250.
16. G. O. Larrazabal, P. Strom-Hansen, J. P. Heli, K. Zeiter, K. T. Therkildsen, I. Chorkendorff and B. Seger, *ACS Appl. Mater. Interfaces*, 2019, **11**, 41281-41288.
17. B. Endrodi, E. Kecsenovity, A. Samu, F. Darvas, R. V. Jones, V. Torok, A. Danyi and C. Janaky, *ACS Energy Lett*, 2019, **4**, 1770-1777.
18. T. Haas, R. Krause, R. Weber, M. Demler and G. Schmid, *Nat. Catal.*, 2018, **1**, 32-39.
19. Z. Liu, H. Yang, R. Kutz and R. I. Masel, *J. Electrochem. Soc.*, 2018, **165**, J3371-J3377.
20. R. B. Kutz, Q. Chen, H. Yang, S. D. Sajjad, Z. Liu and I. R. Masel, *Energy Technol.*, 2017, **5**, 929-936.
21. P. Wei, H. Li, L. Lin, D. Gao, X. Zhang, H. Gong, G. Qing, R. Cai, G. Wang and X. Bao, *Sci. China Chem.*, 2020, **63**, 1711-1715.
22. T. Zheng, K. Jiang, N. Ta, Y. Hu, J. Zeng, J. Liu and H. Wang, *Joule*, 2019, **3**, 265-278.
23. Z. Yin, H. Peng, X. Wei, H. Zhou, J. Gong, M. Huai, L. Xiao, G. Wang, J. Lu and L. Zhuang, *Energy Environ. Sci.*, 2019, **12**, 2455-2462.
24. K. Jiang, S. Siahrostami, T. Zheng, Y. Hu, S. Hwang, E. Stavitski, Y. Peng, J. Dynes, M. Gangisetty, D. Su, K. Attenkofer and H. Wang, *Energy Environ. Sci.*, 2018, **11**, 893-903.